A&A 370, 298–310 (2001)
DOI: 10.1051/0004-6361:20010207

Astronomy & Astrophysics

Modelling of explosive events in the solar transition region in a 2D environment

I. General reconnection jet dynamics

I. Roussev[1], K. Galsgaard[2], R. Erdélyi[3], and J. G. Doyle[1]

[1] Armagh Observatory, College Hill, Armagh, BT61 9DG, N. Ireland
e-mail: ilr@star.arm.ac.uk; jgd@star.arm.ac.uk
[2] School of Mathematics and Statistics, University of St. Andrews, St Andrews, Fife KY16 9SS, Scotland
e-mail: klaus@mcs.st-and.ac.uk
[3] Space & Atmosphere Research Center, Dept. of Applied Mathematics, University of Sheffield, Hicks Building, Hounsfield Road, Sheffield, S3 7RH, UK

Received 13 October 2000 / Accepted 23 January 2001

Abstract. The aim of the present study is to investigate the reconnection jets formed during the process of magnetic flux cancellation in the physical environment of the solar transition region. The emission properties of these jets are then computed for two resonance transition region lines, C IV 1548.2 Å and O VI 1031.9 Å, under the assumption of non-equilibrium ionization. The numerical modelling involves 2-dimensional (2D) dissipative, radiative, nonlinear magnetohydrodynamics. The nonlinear anisotropic thermal conduction, radiative losses, and volumetric heating are taken into account in order to assess their role in the physical situation examined. This work is a continuation of previous related simulations where small-scale energy depositions were modelled in 1D radiative hydrodynamics. Having an X-point reconnection in the mid-transition region gives blue-shifts of the order of ∼100 km s^{-1}, however, the red-shift can be up to one order of magnitude less.

Key words. MHD – Sun: atmosphere – Sun: chromosphere – Sun: UV radiation – Sun: magnetic fields

1. Introduction

A typical whole-Sun image taken by the Yohkoh soft X-ray telescope (SXT) provides us with evidence that the X-ray coronal plasma is maintained at temperatures in excess of 10^6 K. The heating process that generates and sustains the observed hot corona has so far defied a quantitative understanding, despite the multitude of efforts spanning over half a century. The most compelling indication for identifying coronal heating as a magnetic phenomenon is the coincidence of bright X-ray features in the active Sun with magnetic field concentrations (Rosner et al. 1978; Acton et al. 1992). However, the distribution of the magnetic field in the solar atmosphere is not uniform. In many cases, the magnetic field in the solar atmosphere is structured in elongated loop-like forms. The largest contribution to the X-ray emission and to the heating of the corona comes from magnetic loops, identified as the basic building blocks of the solar atmosphere.

To date, two broad-range possibilities for the heating mechanism have been studied: *direct current* (DC) dissipation and *alternating current* (AC) dissipation (e.g., Browning 1991; Narain & Ulmschneider 1996). This division is based on the time scale of the response of the solar corona to the motions of the underlying photosphere (Heyvaerts & Priest 1983; Zirker 1993). When the response of the solar corona consists of slow motions on a time scale long compared to the Alfvén travel time, then the mechanism is called DC. In this case, the magnetic flux tube undergoes a slow evolution and the magnetic energy is gradually built up by shearing motions until the field relaxes, or reconnects to a lower state of energy. A part of the released energy can be converted into heat. Currents that are dissipated in reconnection models of, e.g., micro-flares, explosive events, blinkers and nano-flares are actually believed to be DC currents.

Send offprint requests to: R. Erdélyi,
e-mail: Robertus@sheffield.ac.uk

Suggestions for explaining the high temperature of the solar corona include Alfvén wave dissipation (e.g., Heyvaerts & Priest 1983; Hollweg 1984; Rae & Roberts 1981), turbulent cascades (e.g., van Ballegooijen 1986), current sheet dissipation or nanoflaring (e.g., Parker 1988), and anomalous interruption of field-aligned currents (e.g., Sturrock et al. 1990). As yet, none of these suggestions have proven to be entirely satisfactory.

Table 1. Normalization units

Physical Value	Notation	Typical Value
Length	L_0	$3\ 10^8$ (cm)
Velocity	V_{A0}	$1.829\ 10^7$ (cm s^{-1})
Time	t_{A0}	$1.65\ 10^1$ (s)
Density	ρ_0	$2.51\ 10^{-14}$ (g cm^{-3})
Temperature	T_0	$2\ 10^5$ (K)
Magnetic field	B_0	8 (G)
Thermal Conduction	κ_0	$1.23\ 10^{-6}$ (erg s^{-1} cm^{-1} K^{-1})

High resolution UV spectra taken by the *High Resolution Telescope and Spectrograph* (Brueckner & Bartoe 1983; Dere et al. 1989) revealed very small spatial regions in the solar atmosphere of sudden enhancements in the emission line intensities, associated with strongly broadened non-Gaussian, Doppler shifted line profiles in regions of 2 arcsec or less in size. Similar observations in mid-transition region lines of *SMM UVSP* (see, e.g., Porter et al. 1987) and more recently by *SUMER* (Innes et al. 1997; Perez et al. 1998, 1999; Erdélyi et al. 1997, 1998) and by *TRACE* (Erdélyi et al. 1999, 2001) have confirmed these very localized high-speed events.

Inspired by these observations, and by the work of Parker (1988), Sterling et al. (1991) and Karpen et al. (1995), a numerical study relating the nature of explosive events and their contribution to the coronal heating mechanism was presented by Sarro et al. (1999). A numerical code (called EMMA-D) was developed for the purpose of modelling explosive events in 1D radiative hydrodynamics. In order to fill the gap between theory and observations, an attempt has also been made to convert 1D results into observable line profiles of (E)UV lines, assuming non-equilibrium ionization (Erdélyi et al. 1997; Sarro 1998; Sarro et al. 1999; Teriaca et al. 1999).

Individual explosive events evolve on time scales ranging from 20 to 200 s, and since many events exhibit quite complicated evolution, it is not always possible to assign a single time scale. The histogram of lifetime for explosive events peaks around 40 s. There is now sufficient observational proof that most explosive events are associated with the emergence of new magnetic flux. These observations support the hypothesis that the acceleration of plasma up to the Alfvén velocity (Dere et al. 1991) is due to magnetic field annihilation between the emerging and the pre-existing magnetic field. However, some explosive events cannot be associated with observable changes in the magnetic flux (Dere 1994).

Table 2. A listing of the parameter set used in the present modelling

Parameter	Value
ϵ	7
$\Delta\rho$	4.5
θ	0.6
y_s^*	$0.17\, y_{\max}^*$
y_0^*	$0.17\, y_{\max}^*$
γ	1.667
β	0.164
η_0^*	1/200
α	150
$t_{\rm ri}^*$	5/100
$t_{\rm end}^*$	5

1.1. Numerical modelling of explosive events

The process of magnetic reconnection is a key-issue in the numerous and extensive studies aimed to model phenomena related to active regions, such as solar flares, X-ray jets, etc. (see Yokoyama & Shibata 1996; Forbes et al. 1984; Chen et al. 1999). It was suggested that *fast magnetic reconnection*, i.e. reconnection independent on the plasma resistivity, might be responsible for the burst-like energy release during flare events (see Magara et al. 1996, 1997; Magara & Shibata 1999). It was found that models of solar flares involving fast magnetic reconnection match to a very high extend some recent X-ray observations taken by Yohkoh.

Although the spatial and time scales, as well as plasma densities and temperatures, involved in flare events are different from the ones representing the "quiet" Sun transition region, the general description of the magnetic reconnection problem is similar. The magnetic fields involved in the "quiet" Sun network are also by orders of magnitude weaker than the ones in active regions. It is still unclear, however, whether the current "sheets" formed in the quiet Sun fulfill the requirements of triggering fast magnetic reconnection, as the electric current densities involved are much lower than the ones for active regions. Since explosive events are observed as high-velocity events, but not as high-density events, a hint about the low mass densities involved in the diffusion site becomes straightforward, if of course magnetic reconnection is responsible for the occurrence of the phenomenon. Separate studies are therefore needed to model transient events in the quiet Sun, and in particular explosive events, since these involve particular physical environments.

In contrast to 2D MHD simulations of explosive events, there has been a significant progress in numerical simulations in 1D HD and in particular, computing observable consequences. Sarro et al. (1999) simulated the evolution of UV emission line profiles (e.g., C IV) of small-scale

energetic transients (e.g., explosive events). The same idea has been used to model the long-standing problem of transition region line-shifts (Teriaca et al. 1999). In these studies it has became clear that radiative MHD is needed for a better understanding of the development of the blue- and red-shifted jets (Sterling et al. 1991; Karpen et al. 1995).

The interaction between a newly emerging magnetic flux and the pre-existing coronal field was numerically modelled by Jin et al. (1996) and Innes & Tóth (1999) in 2D MHD. Although the physical models involved in these simulations showed a high degree of sophistication in the dynamics of the events, effects due to radiative losses, volumetric heating and thermal conduction were not included.

In the present study we aim to investigate the reconnection jets caused by a process of magnetic reconnection in a 2D physical environment representing the solar transition region. Magnetic flux cancellation is initiated by a localized increase of the magnetic diffusivity in the current concentration. In addition, we have performed line synthesis in two representative transition region lines, C IV 1548.2 Å and O VI 1031.9 Å (where explosive events are often observed), under the assumption of non-equilibrium ionization. This line synthesis, however, is carried out in 1D and involves only the direction along which the utmost jet velocities are reached during the whole 2D MHD experiment. As a result, velocity events are identified and referred to explosive events in the time series of both lines.

2. Physical description of the problem

2.1. Basic equations

In the present study we consider a solar atmosphere represented by ideal gas in the presence of magnetic field. For simplicity, the effects of gravity are neglected. The governing equations of a 2D dissipative, radiative MHD are

$$\frac{D\,\rho}{D\,t} = -\rho\,\nabla\cdot\boldsymbol{U}, \tag{1}$$

$$\rho\,\frac{D\,\boldsymbol{U}}{D\,t} = -\nabla\,P + \boldsymbol{j}\times\boldsymbol{B} - \nabla\cdot\hat{\tau}, \tag{2}$$

$$\nabla\cdot\boldsymbol{B} = 0, \tag{3}$$

$$\frac{\partial\,\boldsymbol{B}}{\partial\,t} = \nabla\times(\boldsymbol{U}\times\boldsymbol{B}) - \nabla\times[(\eta+\eta_{\rm loc})\,\nabla\times\mathbf{B}], \tag{4}$$

$$\begin{aligned}\frac{\partial\,e}{\partial\,t} = \;& -\nabla\cdot(e\,\boldsymbol{U}) - P\,\nabla\cdot\boldsymbol{U} + Q_{\rm visc} + Q_{\rm Joule} \\ & -\nabla\cdot\boldsymbol{q} - L_{\rm r} + S,\end{aligned} \tag{5}$$

where $D/Dt \equiv \partial/\partial t + \boldsymbol{U}\cdot\nabla$, and ρ, P, $\boldsymbol{U}$, $\boldsymbol{B}$, $\boldsymbol{j}$, η, $\hat{\tau}$, $e = P/(\gamma-1)$, $Q_{\rm visc}$, $Q_{\rm Joule}$, $\boldsymbol{q}$, S, $L_{\rm r}$ are the mass density, kinetic gas pressure, fluid velocity, magnetic field, electric current density, magnetic diffusion coefficient (numerical), viscous stress tensor (numerical), internal energy, viscous dissipation, Joule dissipation, heat flux, volumetric heating rate, and radiative losses, respectively. Here by $\eta_{\rm loc}$ we denote a coefficient of localized magnetic diffusion used in our experiments to initiate magnetic reconnection. In addition $\boldsymbol{j}$, P, $\boldsymbol{q}$, and $L_{\rm r}$, are explicitly given by

$$\boldsymbol{j} = \nabla\times\boldsymbol{B}, \text{ and } P = \rho\,T, \tag{6}$$

$$\boldsymbol{q} = -\kappa_{\parallel}\,\nabla_{\parallel}\,T, \text{ and } L_{\rm r} = n_{\rm e}\,n_{\rm p}\,Q(T). \tag{7}$$

Here $\kappa_{\parallel}$ is the thermal conduction along the magnetic field which is given by $\kappa_{\parallel} = \kappa_0 T^{5/2}$. Subscript $\parallel$ in the nabla operator refers to values along the magnetic field, $n_{\rm e}$ is the electron number density, and $n_{\rm p}$ is the proton number density. We also work in units where the gas constant $R_0 = \mu$ (the mean molecular weight), and the magnetic permeability μ_0 is set to 1. For the radiative loss function, $Q(T)$, we choose the form given by Cook et al. (1989), calculated assuming photospheric abundance. A series of second order polynomial fits to $Q(T)$ are given in Appendix A.

2.2. Initial state

Initially, we consider a magnetic field which is parallel to the $y-$axis, and defined by

$$\boldsymbol{B} = (0, B_y);\;\; B_y = B_0\tanh\left(25\,\frac{x}{L_0}\right). \tag{8}$$

Here L_0 and B_0 are typical values of a length scale and magnetic field strength, respectively. We consider a physical domain of size $[6\,L_0, 6\,L_0]$, where $-3\,L_0 \le x \le 3\,L_0$, and $-3\,L_0 \le y \le 3\,L_0$.

Since there is a steep gradient of the magnetic field in the $x-$direction, there will be a thin current concentration formed along the $y-$direction. The initial velocity field is assumed to be zero throughout the computational domain, and therefore we refer to a static equilibrium state, i.e., $\boldsymbol{U} = 0$.

The third basic assumption refers to the total pressure balance in the entire domain, i.e.

$$\frac{B^2}{2} + P = \frac{B_0^2}{2} + P_0 = \text{const.} \tag{9}$$

Furthermore, we assume the kinetic gas pressure P to be a fraction of the magnetic pressure $P_{\rm m} = B^2/2$, given through the plasma beta parameter $\beta = P/P_{\rm m}$. The latter is assumed to be uniform in the $y-$direction (i.e., height in the solar atmosphere). As a result, the thermal energy $e = P/(\gamma-1)$ is also uniform in the $y-$direction (although in reality it decreases in height towards the solar corona). Across the current concentration, the magnetic field changes its polarity; the magnetic pressure also changes its magnitude. Taking into account the condition for total pressure balance in the entire domain, we derive the following dependence of the thermal energy e on the $x-$coordinate

$$e(x,y) = e(x) = e_0\left[\frac{1+\beta-\left(\frac{B_y}{B_0}\right)^2}{\beta}\right]. \tag{10}$$

In order to represent a solar transition region, we assume the following profile of the mass density ρ in the $y-$direction

$$\rho(y) = \rho_0 \left\{1 + \Delta\rho \left\{1 - \tanh\left[\frac{\epsilon}{L_0}(y + y_s)\right]\right\}\right\}. \quad (11)$$

Here ρ_0 represents a typical value of the mass density in the low density region and $2\Delta\rho$ defines the relative density jump across the transition region. The parameter ϵ describes the steepness of the transition region. Furthermore, y_s is used to shift the position of the density profile in the numerical domain. Since the kinetic gas pressure is considered to be uniform in the $y-$direction, the corresponding temperature profile is represented by an increasing function in height, and given through the relation $T(y) = P/\rho(y)$.

Regarding the profile of the mass density $\rho(x)$ across the current concentration (in the $x-$direction), we adopt the following parametric representation

$$\rho(x) = \rho_0 \left(\frac{P}{P_0}\right)^{\theta} = \rho_0 \left(\frac{e}{e_0}\right)^{\theta}, \quad (12)$$

where θ is a free parameter (1 over the polytropic index) used to control the density profile in the current concentration. After taking into account Eq. (10), the density profile becomes

$$\rho(x) = \rho_0 \left[\frac{1 + \beta - \left(\frac{B_y}{B_0}\right)^2}{\beta}\right]^{\theta}. \quad (13)$$

The 2D profile of the mass density is derived to be $\rho(x,y) = \rho(x)\rho(y)/\rho_0$, and is explicitly given by

$$\rho(x,y) = \rho_0 \left[\frac{1 + \beta - \left(\frac{B_y}{B_0}\right)^2}{\beta}\right]^{\theta} \times \left\{1 + \Delta\rho \left\{1 - \tanh\left[\frac{\epsilon}{L_0}(y + y_s)\right]\right\}\right\}. \quad (14)$$

Using the equations of state $e = \rho T/(\gamma - 1)$, Eq. (10) and Eq. (14), we derive the 2D temperature profile $T(x,y)$ to be

$$T(x,y) = T_0 \left[\frac{1 + \beta - \left(\frac{B_y}{B_0}\right)^2}{\beta}\right]^{1-\theta} \times \left\{1 + \Delta\rho\left\{1 - \tanh\left[\frac{\epsilon}{L_0}(y + y_s)\right]\right\}\right\}^{-1}. \quad (15)$$

The last basic assumption made for the initial state refers to an energy balance in the entire physical domain. Using Eq. (6) this energy balance reads

$$S(x,y) - \nabla \cdot \boldsymbol{q}(x,y) - L_r(x,y) = 0; \quad \text{at} \quad t = 0, \quad (16)$$

which automatically defines the background heating rate through the radiative losses derived for the initial state and the divergence of the initial heat flux.

2.3. Driver of magnetic reconnection

In order to initiate magnetic reconnection in the system, and therefore to allow the magnetic field to dissipate, we introduce a localized magnetic diffusion (see Eq. (4)). Hence, a local increase of the magnetic diffusivity, $\eta_{\rm loc}$, is assumed and assigned for a finite time

$$\eta_{\rm loc}(x,y;t) = \eta_0 F(t) \exp\left\{-\frac{\alpha}{L_0^2}\left[x^2 + (y + y_0)^2\right]\right\}, \quad (17)$$

where

$$F(t) = \begin{cases} \frac{t}{t_{\rm ri}}, & 0 \le t \le t_{\rm ri}, \\ 1, & t_{\rm ri} < t \le t_{\rm end}, \\ 0, & t_{\rm end} < t. \end{cases} \quad (18)$$

Here η_0 is the normalized value of the magnetic diffusion coefficient defined as the reciprocal of the magnetic Reynolds number, R_m, i.e. $\eta_0 = V_{A0}L_0/R_m$ (where V_{A0} is the Alfvén speed given by $V_{A0} = B_0/\sqrt{\rho_0}$). The spatial shape of $\eta_{\rm loc}$ is described as a double Gaussian, and is defined through the parameter α. The coefficient of localized magnetic diffusion represented by Eq. (17) linearly increases from time $t = 0$ to $t = t_{\rm ri}$ (where t and $t_{\rm ri}$ are given in units of the Alfvén travel time $t_{A0} = L_0/V_{A0}$), followed by a constant value up to $t = t_{\rm end}$. At time $t = t_{\rm end}$ the localized magnetic diffusivity is set to zero.

The introduction of $\eta_{\rm loc}$ for a finite time in the center of the current concentration forces the magnetic field on either side of the current concentration to start reconnecting. This process changes the topology of the magnetic field from the initial 1D current concentration along the $y-$axis into a 2D X-point. The formation of the X-point initiates a traditional 2D reconnection situation where magnetic flux is advected into the X-point along the $x-$axis, and is being expelled from the diffusion region through two reconnection jets (along the $y-$axis of the domain). It is the magnetic tension force in the reconnected magnetic field lines that accelerates the plasma along the current concentration and away from the diffusion region. The aim of the present study is to investigate in detail the dynamics of these jets. The initiation of the reconnection outflow causes a decrease in the total pressure at the X-point, and an inflow is dynamically created as a reaction to the change in the force balance around the X-point.

2.4. Dimensionless equations and parameters

The dimensionless physical quantities and parameters of the problem are defined as follows

$$V_{A0} = \frac{B_0}{\sqrt{\rho_0}}, \quad t_{A0} = \frac{L_0}{V_{A0}}, \; T_0 = (\gamma - 1)\frac{e_0}{\rho_0}, \quad e_0 = \frac{\beta}{(\gamma - 1)}\frac{B_0^2}{2}; \quad (19)$$

$$x^* = \frac{x}{L_0}, \; y^* = \frac{y}{L_0}, \; t^* = \frac{t}{t_{A0}}, \; u = \frac{\boldsymbol{U}}{V_{A0}}; \quad (20)$$

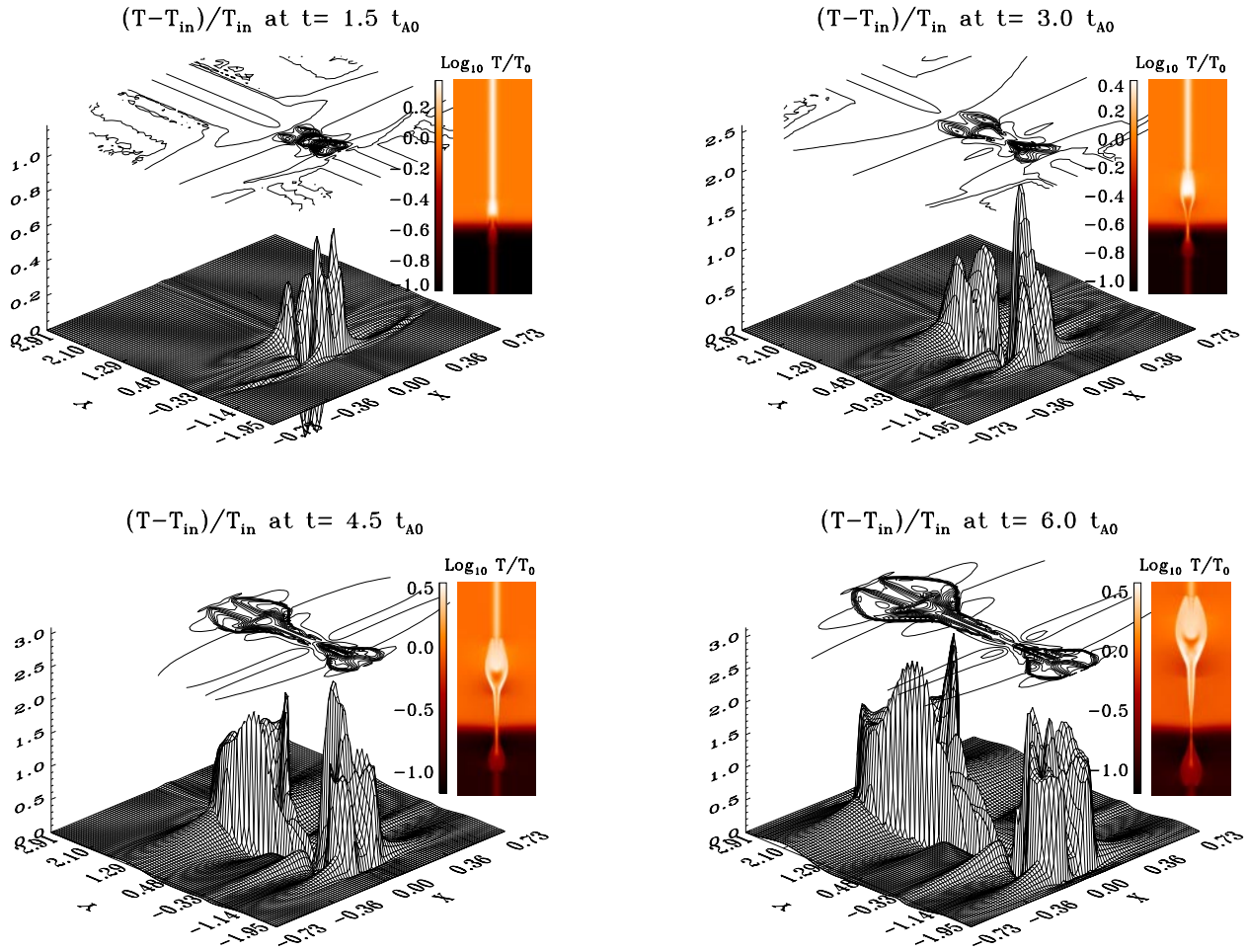

Fig. 1. Relative changes in the temperature, $(T - T_{\rm in})/T_{\rm in}$, with respect to the initial temperature field, $T_{\rm in}$, are shown at four times: $t = 1.5\,t_{\rm A1}$, $3.0\,t_{\rm A1}$, $4.5\,t_{\rm A1}$, and $6.0\,t_{\rm A1}$, respectively. The image plot at the top right corner of each figure represents the logarithm of the temperature $\log_{10}(T/T_0)$ at given time (see text for more details)

$$\rho^* = \frac{\rho}{\rho_0},\ T^* = \frac{T}{T_0},\ \boldsymbol{b} = \frac{\boldsymbol{B}}{B_0},\ e^* = \frac{e}{e_0}; \tag{21}$$

and

$$j^* = \frac{j}{j_0},\quad \text{where}\quad j_0 = \frac{B_0}{L_0}. \tag{22}$$

Here L_0, ρ_0, T_0, e_0, and B_0 are typical representative values of a length scale, mass density, temperature, thermal energy, and magnetic field strength above the transition region in the model. The current density, $\boldsymbol{j}$, is represented by its only non-zero component, the $z-$component, which we denote by j.

The numerical domain considered here is of size $[2\,x^*_{\rm max}, 2\,y^*_{\rm max}]$, where $-x^*_{\rm max} \le x^* \le x^*_{\rm max}$, $-y^*_{\rm max} \le y^* \le y^*_{\rm max}$, and $x^*_{\rm max} = y^*_{\rm max} = 3$.

In terms of the dimensionless physical quantities and parameters of the problem, the initial state reads

$$\boldsymbol{u} = 0, \tag{23}$$

$$b_x = 0,\ b_y = \tanh(25\,x^*), \tag{24}$$

$$e^* = \frac{1}{2(\gamma-1)}\,(1 + \beta - b_y^2), \tag{25}$$

$$\rho^* = \left[\frac{(1+\beta-b_y^2)}{\beta}\right]^{\theta} \times \{1 + \Delta\rho\,\{1 - \tanh[\epsilon\,(y^* + y^*_{\rm s})]\}\}, \tag{26}$$

and

$$T^* = (\gamma - 1)\,\frac{e^*}{\rho^*}. \tag{27}$$

The dimensionless form of the localized magnetic diffusivity, $\eta_{\rm loc}$, is derived to be (cf. Eq. (17))

$$\eta^*_{\rm loc}(x^*, y^*; t^*) = \eta^*_0\,F^*(t^*) \times \exp\left\{-\alpha\,\left[x^{*2} + (y^* + y^*_{\rm s})^2\right]\right\}, \tag{28}$$

where

$$\eta^*_0 = \frac{\eta_0}{L_0\,V_{\rm A0}}, \tag{29}$$

and

$$F^*(t^*) = \begin{cases} \frac{t^*}{t^*_{\rm ri}}, & 0 \le t^* \le t^*_{\rm ri}, \\ 1, & t^*_{\rm ri} < t^* \le t^*_{\rm end}, \\ 0, & t^*_{\rm end} < t^*. \end{cases} \tag{30}$$

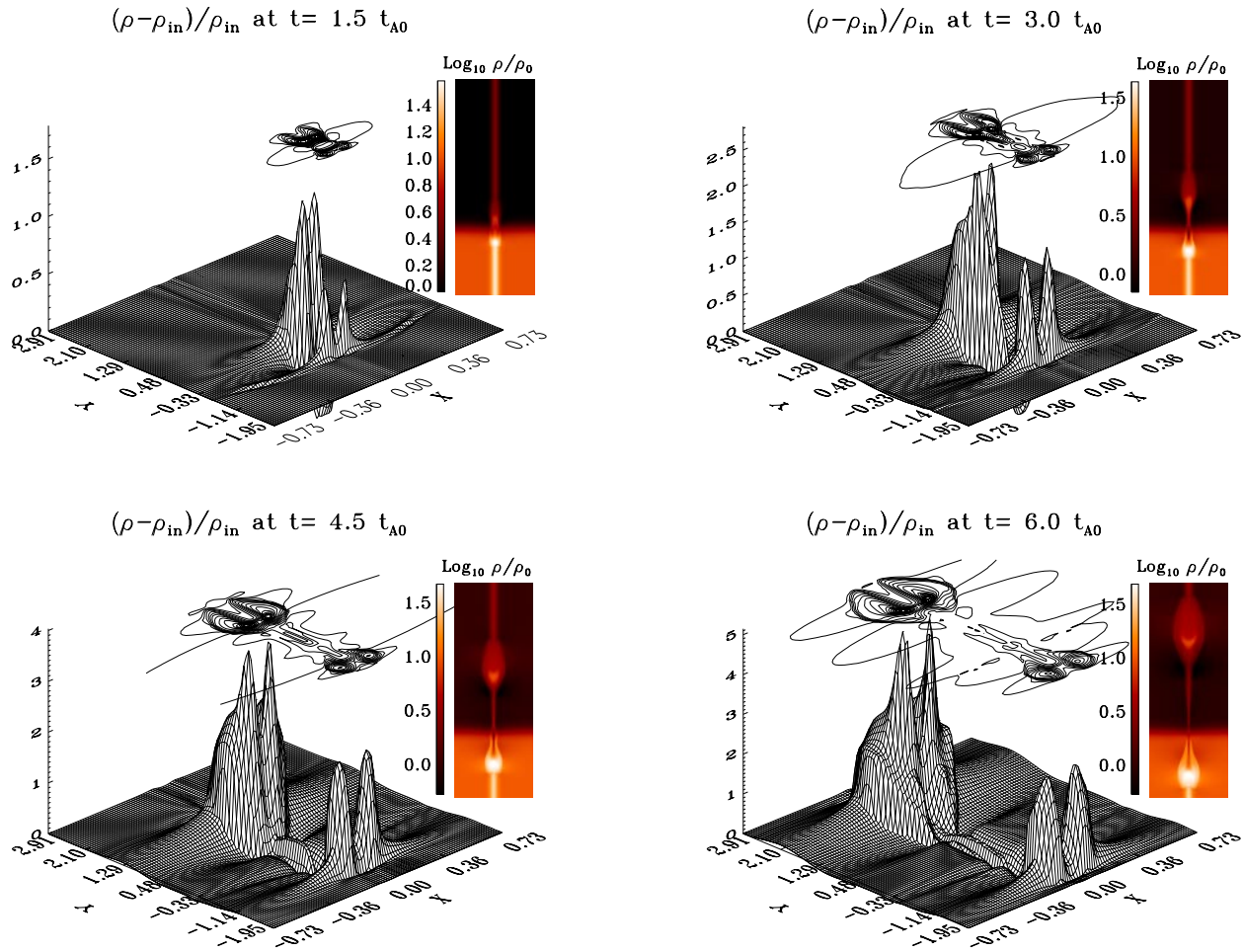

Fig. 2. Relative changes in mass density, $(\rho - \rho_{\rm in})/\rho_{\rm in}$, with respect to the initial density distribution, $\rho_{\rm in}$, are shown at four times: $t = 1.5\,t_{\rm A1}$, $3.0\,t_{\rm A1}$, $4.5\,t_{\rm A1}$, and $6.0\,t_{\rm A1}$, respectively. The image plot at the top right corner of each figure represents the logarithm of the mass density $\log_{10}(\rho/\rho_0)$ at the given time (see text for more details)

Here $t^*_{\rm ri} = t_{\rm ri}/t_{\rm A0}$ and $t^*_{\rm end} = t_{\rm end}/t_{\rm A0}$.

The energy balance for the initial state written in dimensionless form reads (cf. Eq. (16))

$$S^* - \nabla^* \cdot \boldsymbol{q}^* - L^*_{\rm r} = 0; \quad \text{at} \quad t^* = 0, \tag{31}$$

where $\nabla^* = L_0 \nabla$,

$$S^* = \frac{S}{S_0}, \; S_0 = \frac{\rho_0\, V^2_{\rm A0}}{t_{\rm A0}}, \tag{32}$$

$$\boldsymbol{q}^* = -\kappa^*_{\parallel}\, \nabla^*_{\parallel}\, T^*, \quad \kappa^*_{\parallel} = \hat{\kappa}\, T^{*5/2}, \text{ and} \tag{33}$$

$$\hat{\kappa} = \kappa_0\, T_0^{7/2}\, \frac{t_{\rm A0}}{\rho_0\, V^2_{\rm A0}\, L^2_0}.$$

Also, the dimensionless form of the radiative loss function, $L^*_{\rm r}$, is given by

$$L^*_{\rm r} = \rho^{*2}\, Q^*(T), \quad \text{where} \tag{34}$$

$$Q^*(T) = 0.852\, \frac{\rho_0\, t_{\rm A0}}{m_p^2\, V^2_{\rm A0}}\, Q(T).$$

Here $m_{\rm p}$ is the proton mass, and the factor 0.852 comes from the assumed ratio between the electron and proton number density $n_{\rm e}/n_{\rm p}$. The values of the normalization units adopted in this study are summarized in Table 1. These values refer to the high temperature region outside the current concentration (i.e. $(x^*, y^*) = (-x^*_{\rm max}, y^*_{\rm max})$).

2.5. Parameter set in the model

In the present study we examine the response of a 2D physical environment, representing the solar transition region, to a magnetic reconnection event initiated inside the transition region at location y^*_0. We consider the general case when there is a mass density concentration at the current concentration ($\theta \neq 0$ in Eq. (12)) formed between the two vertical magnetic fluxes of opposite polarity. The exact parameter set used in the model is given in Table 2.

This model represents the physical situation when two magnetic flux tubes of opposite polarity are pushed together and contact each other due to their foot-point motions. This initiates magnetic reconnection and the generation of two oppositely propagating jets: one propagating towards the corona (high temperature region), and another moving towards the chromosphere (high density region).

Let us here discuss the magnetic Reynolds numbers, $R_{\rm m}$, involved in our modelling. A representative value of $R_{\rm m}$ for the physical environment of the solar transition region can be derived using the classical arguments given by Mariska (1992). Using the normalization units given in Table 1, as representative for the "quiet" Sun transition

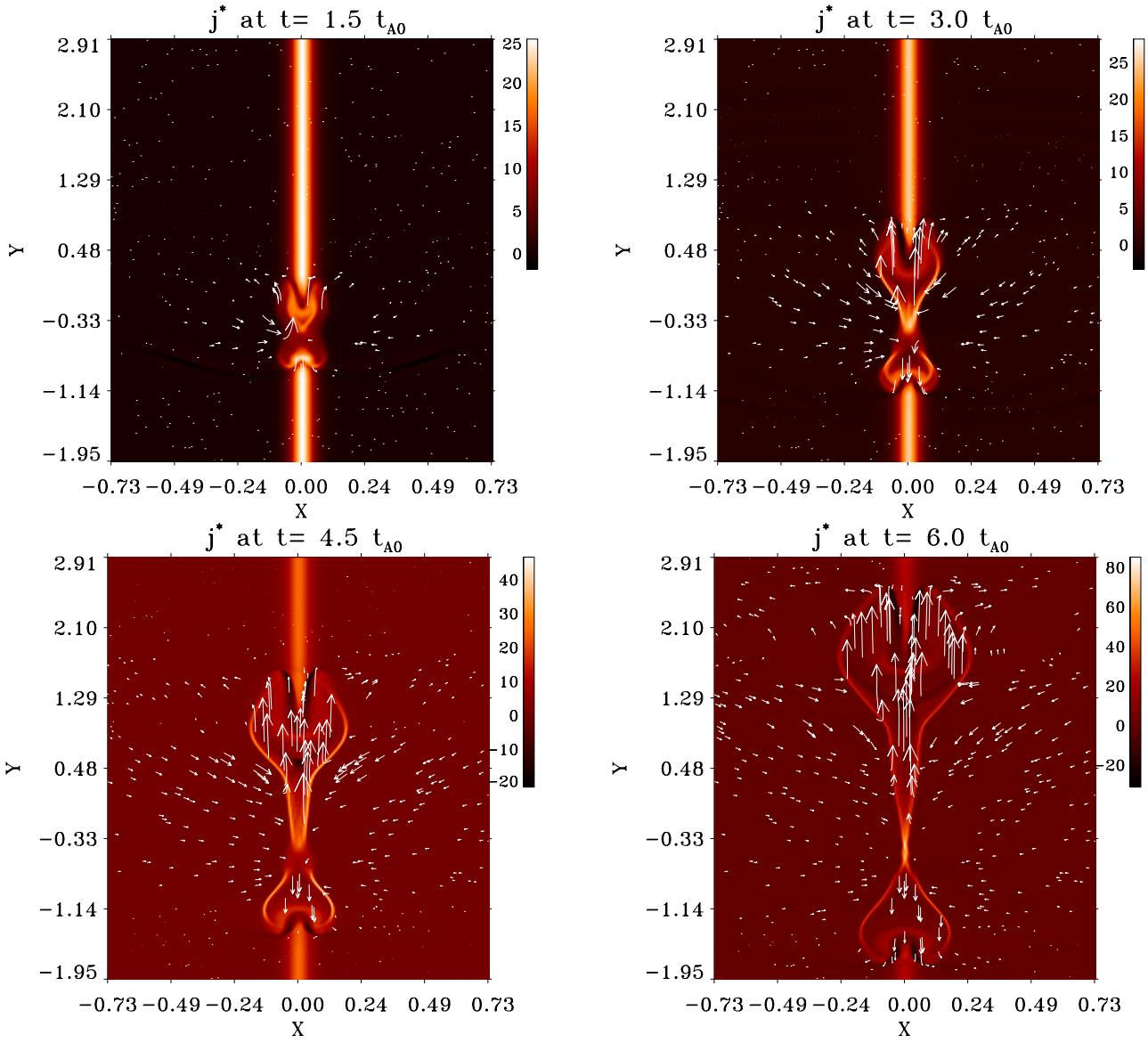

Fig. 3. Images of the $z-$component of the current, j^*, are shown at the same times as in Fig. 1. Short streak lines represent the velocity field at a given time

region, one can derive $R_{\rm m}^{\rm cl} \approx 10^8$. The magnetic Reynolds number (see Table 2) corresponding to the peak value of the localized magnetic diffusivity, however, is taken to be 200 (note $R_{\rm m} = 1/\eta_0^*$). The latter value is a few orders of magnitude less than $R_{\rm m}^{\rm cl}$. On the one hand, there is no observational clue that could give us an idea of what magnetic Reynolds numbers are be involved in the solar plasma before the process of magnetic reconnection takes place. On the other hand, the magnetic diffusion region in a steady state reconnection is represented by $R_{\rm m} = 1$. Thus, in order to get reconnection rates that will match the observed dynamical time scales of explosive events for example, one definitely needs to assume $R_{\rm m} \ll R_{\rm m}^{\rm cl}$.

We believe the answer to this critical issue regarding $R_{\rm m}$ will be reached by performing numerical simulations that best match observations indicating magnetic reconnection.

3. Numerical method

The numerical experiments are performed using a 2D compressible MHD code based on staggered meshes. The MHD equations, Eqs. (1)–(7), are solved in a 2D domain using non-uniform staggered grids. The grids are stretched in the $x-$direction to better resolve the region around the current concentration in which the important dynamics of the experiment take place. At the same time the

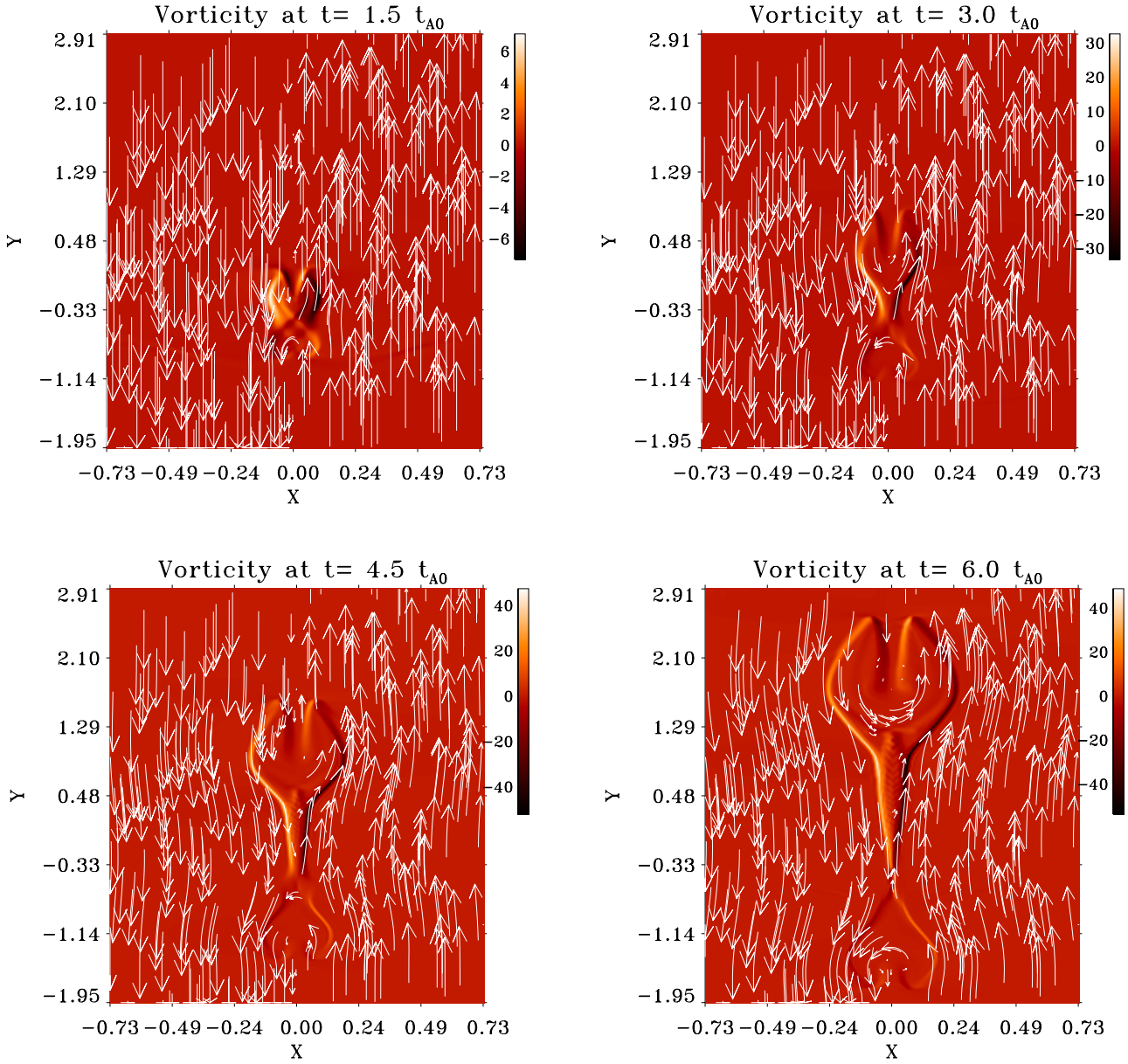

Fig. 4. Vorticity of the velocity field at the same times as in Fig. 1 is shown. In addition, short field lines are plotted to represent the magnetic field topology (see text for details)

stretching of the grid moves the $x-$boundaries far enough away in order to not influence the results.

The MHD code used in our experiments conserves mass, momentum, energy, and magnetic field divergence. In order to derive the partial derivatives in the MHD equations, a sixth-order method is applied. The interpolation of various functions between the grids are done using a fifth-order method. Viscosity and magnetic resistivity are both handled using a combined second and fourth-order method extended with a discontinuous capture mechanism, in order to provide the highest possible spatial resolution for a given numerical resolution. The solution is advanced in time using a third-order predictor-corrector method. The code is able to dissipate efficiently when the physics generates structures (such as current sheets) at the smallest resolved scales. The dissipation on well resolved scales is kept as small as possible in order to increase the effective numerical resolution of the code. However, realistic values of neither the Reynolds nor the magnetic Reynolds numbers have been reached in these numerical experiments. A description of the code (by Nordlund & Galsgaard) is available at `http://www-solar.mcs.st-and.ac.uk/~klaus`.

The boundaries are taken to be ideally conducting and impenetrable, with the parallel velocity at the boundaries kept as zero throughout the experiments. We are working at present on implementing open boundary conditions.

4. Discussion on the numerical results

This section discusses the results obtained from the numerical experiment presented above. Section 4.1 is dedicated to the general dynamics of the physical situation

examined. The line synthesis part of this study is described in Sect. 4.2 where final conclusions are also drawn.

4.1. General dynamical evolution

The model experiment described in Sect. 2 is carried out in a stretch grid (see Sect. 3 for details), where stretching is applied only in the $x-$direction (across the current concentration) in order to assess very high resolution in resolving the current concentration. In the $y-$direction, however, there is no stretching applied since we need high resolution all the way through in that direction. The grid-size used is $N_x \times N_y = 400 \times 700$, where 50% of the grid points in the $x-$direction are located within $-0.7 \leq x \leq 0.7$, which is 0.23 times the $x-$size of the domain. The localized magnetic diffusivity is switched on at time $t = 0$, and is maintained until time $t = 5.0\, t_{\rm A0}$. The experiment itself is continued until time $t = 6.0\, t_{\rm A0}$, which in absolute units corresponds to $t = 99$ s.

Once the localized magnetic diffusivity starts increasing, the magnetic field begins to dissipate and the initial force balance is destroyed. The dissipation of the magnetic field generates a 2D X-point topology centered on the localized magnetic diffusivity patch. The newly reconnected field lines possess a strong tension force in the $\pm\, y-$direction, and start to pull out plasma from the diffusion region along the current concentration in either direction. As a reaction to the decrease in the plasma and magnetic forces in the diffusion region, an inflow of magnetized plasma from the surroundings outside the current concentration is initiated. This inflow advects new flux into the diffusion region, and as the reconnection proceeds, the outflow jets continue to accelerate along the $y-$direction.

The temperature and density structure of the current concentration, as the two jets evolve, are shown in Figs. 1 and 2. Each figure includes four snapshots taken at equal intervals of time. Figure 1 shows the relative changes in the temperature, $(T-T_{\rm in})/T_{\rm in} = (T^*-T^*_{\rm in})/T^*_{\rm in}$, with respect to the initial temperature field, $T_{\rm in}$, at time: $t = 1.5\, t_{\rm A1}$ $3.0\, t_{\rm A1}$, $4.5\, t_{\rm A1}$, and $6.0\, t_{\rm A1}$, respectively. In order to present better the fine structure of the current concentration, we show only the $-.73 \leq x^* \leq .73$ interval in the $x-$direction, and $-1.95 \leq y^* \leq 2.9$ in the $y-$direction. On the surface and contour plots this rectangular domain is compressed in the $x-$direction, and a square domain is shown. The adjacent image plots show the logarithm of temperature, $\log_{10}(T/T_0)$, in the correct aspect ratio between the two axes. Similar plots are made for the mass density, and Fig. 2 shows the relative changes in the mass density, $(\rho - \rho_{\rm in})/\rho_{\rm in} = (\rho^* - \rho^*_{\rm in})/\rho^*_{\rm in}$, with respect to the initial density distribution, $\rho_{\rm in}$, at the same times as in Fig. 1. Here the image plots represent the logarithm of the mass density, $\log_{10}(\rho/\rho_0)$. Both Figs. 1 and 2 clearly show a double-peak structure of each jet in the relative changes, while single peaks are seen in the absolute values of the temperature and mass density. This difference is due to the profile of the initially enhanced density and temperature in the current concentration and the increasing width of the jet front.

The thermal energy of the two jets increases with time, while it gradually decreases at the X-point. Due to the fast expansion of the hot jets, the non-heated plasma surrounding the current concentration is pushed away. In connection with this, two high density plasma concentrations develop (see the grey-scale images of Fig. 2). Since the plasma β outside the current concentration is less than unity (i.e., $\beta = 0.164$), the increased kinetic gas pressure in the two jets can be balanced only by a small perturbation of the magnetic field in the direction perpendicular to the current concentration. Therefore, the expansion of the jet plasma in the $x-$direction is smaller than in the $y-$direction.

As expected, the jet propagating towards the high temperature region ("blue-jet" hereafter) reaches a higher velocity than the one moving towards the high density region ("red-jet" hereafter). The "blue-jet" propagates towards a region with decreasing mass density and increasing temperature, while for the "red" one the physical situation is the other way around. Therefore, as the Lorenz forces available for accelerating the plasma of the two jets are of the same magnitude, the acceleration of the "blue-jet" will be higher than the one the "red-jet" experiences. Both jets reach supersonic and super Alfvénic velocities along the axis $x = 0$, and bow shocks are formed at the front of each jet. As the distance to the symmetry axis in the $x-$direction is increased, the sound speed decreases while the Alfvén speed increases in the initial background plasma. The bow shocks therefore become less steep, and at a given $x-$distance they change to be only supersonic. The image plots in Fig. 1 reveal the "tulip-like" structure of the "blue-jet", where a relatively "cold" region inside the core is recognized. From the density images in Fig. 2 it is seen that the same region contains dense plasma.

A detailed picture of the velocity field, at the same four times as in Fig. 1, is shown in Fig. 3 as short streak lines. Note these are plotted with random starting points, though the velocity field is symmetric with respect to $x = 0$. The background shading in the figures represents the current density. The locations of strong current clearly show the positions of the slow MHD shocks. The velocity flow is found to have a slightly converging pattern close to the X-point and the reconnection event would therefore, in a steady state case, be classified as a Petschek type according to Priest & Forbes (1986).

The corresponding changes in the magnetic field topology are shown in Fig. 4. Here the magnetic field is plotted as short field line traces, while the background images represent vorticity. Both are given again at the same four times as in Fig. 1. Note again that the magnetic field has a symmetric pattern with respect to $x = 0$, though the short field lines representing it are randomly plotted. The vorticity shows the locations of rapid changes in the direction of the fluid velocity. From the quadrupolar structure of the vorticity one can easily see the location of the

X-point, as well as recognize the separators across which the magnetic field changes connectivity. The locations of sharp changes in the fluid velocity, i.e. strong vorticity, also indicate where strong electric current is accumulated as well as where slow mode shocks are formed.

In trying to classify this type observationally, we note that the relative density and temperature changes, as well as the absolute value of mass density and temperature at the location of maximum jet velocity are given in Table 3. By $\delta\rho^b_{\rm jet} = (\rho^b_{\rm jet} - \rho_{\rm in})/\rho_{\rm in}$ we denote the value of the relative density changes at the location of maximum jet velocity, $\rho^b_{\rm jet}/\rho_{\rm in}$ is the jet density in units of the initial density $\rho_{\rm in}$ at that location, and $\rho^b_{\rm jet}/\rho_0$ is the jet density in units of the normalization value of the mass density ρ_0. In a similar way this is done for the temperature.

Table 3. Values of various quantities at the maximum $V_{\rm jet}$ locations

Quantity	Time $1.5t_{\rm A1}$	Time $3.0t_{\rm A1}$	Time $4.5t_{\rm A1}$	Time $6.0t_{\rm A1}$
$V^b_{\rm jet}/V_{\rm A0}$	0.24	0.50	0.85	0.99
$\delta\rho^b_{\rm jet}$	0.46	0.63	−0.11	−0.30
$\rho^b_{\rm jet}/\rho_{\rm in}$	1.46	1.63	0.89	0.70
$\rho^b_{\rm jet}/\rho_0$	6.91	5.36	2.85	2.25
$\delta T^b_{\rm jet}$	−0.46	−0.61	−0.35	−0.10
$T^b_{\rm jet}/T_{\rm in}$	0.54	0.39	0.65	0.90
$T^b_{\rm jet}/T_0$	0.79	0.83	1.41	1.96
$V^r_{\rm jet}/V_{\rm A0}$	0.09	0.20	0.22	0.24
$\delta\rho^r_{\rm jet}$	−0.26	−0.86	−0.85	−0.83
$\rho^r_{\rm jet}/\rho_{\rm in}$	0.74	0.14	0.15	0.17
$\rho^r_{\rm jet}/\rho_0$	21.73	3.79	4.65	4.95
$\delta T^r_{\rm jet}$	0.43	2.27	2.65	1.76
$T^r_{\rm jet}/T_{\rm in}$	1.43	3.27	3.65	2.76
$T^r_{\rm jet}/T_0$	0.34	0.84	0.83	0.68

Since the mass density at the location of maximum jet velocity in units of the initial density, $\rho^b_{\rm jet}/\rho_{\rm in}$, is not more than 1.63 for the "blue-jet", and 0.74 for the 'red-'one (see rows 3 and 10 in Table 3), it is to be expected that we obtain 'velocity events' rather than "density events". This is the first hint that these numerical results might be related to the solar explosive events, since observations reveal explosive events as being high-velocity events rather than being high density events (Teriaca et al. 2000).

At this stage, there is an interesting conclusion to be drawn. At the locations of the maximum jet velocity, the relative and absolute changes in both mass density and temperature are not very "dramatic". This gives us a hint about the possible visibility of the two jets at the resonance transition region lines, as they are formed in a narrow temperature band. Therefore, since the high velocity regions of the two jets do not undergo significant changes in temperature, and also because of being relatively denser than the surrounding material, they may become visible as two high velocity satellites in the line profiles of resonance transition region lines.

Finally, the implications of the thermal conduction, radiative losses and the background heating included in our model were tested by running an experiment with a different reference temperature, $T_0 = 1\ 10^5$ K. By comparing these, it is found that the general dynamics of the two experiments are very similar, but with the implications that the temperature and density values are important for the formation of the resonance transition region lines discussed in the next section. This is not surprising since, for example, in the solar corona the radiative losses are expected to be less important than the heat conduction, while the situation in the chromosphere is opposite. The complicated interaction between these two processes makes it difficult to predict their net effect on the model situation presented in this paper. First, the radiative loss peaks at transition region temperatures. Second, the source and distribution of the background heating is still unknown. Therefore, one can speculate about the impact on a dynamical event that takes place in the solar transition region. Generally speaking, the role of thermal conduction in the formation of the two jets would then be to slightly increase the mass density of their hottest parts by decreasing their temperature. The radiative losses, in turn, may cool the colder parts of the jets faster than the hot ones and therefore increase the density here. Which process is the most dominant therefore depends on the actual physical conditions and the time scales for the relevant processes.

Here we would like to stress the fact that, although our 2D model situation represents a temperature transition region, the temperature (density) structure was defined first, and then the background heating rate was derived using the energy equation for the initial state (cf. Eq. (16)). In a follow-up study we intend to construct an initial state in which explicit assumptions about the background heating are made first, and then derive the corresponding temperature (density) stratification in a more consistent way. This would be a better approach in defining a 2D physical environment representing the solar transition region. Furthermore, such an approach will certainly have an impact on the importance of the thermal conduction and radiative losses to the physics involved in the numerical modelling. Recall the coronal heating problem addressed in Sect. 1, all this may become a key-issue in any further related study dedicated to calculate the contribution of explosive events to the coronal heating. We believe that numerous small scale transient events on the "quiet" Sun, like explosive events, could significantly contribute to the heating of the solar atmosphere.

The results about the general jet dynamics presented here are in agreement with some recent studies (see Jin et al. 1996; Innes & Toth 1999), involving similar reconnection models relevant to explosive events. The line synthesis performed in these studies, however, did not take into account any departure from the ionization equilibrium of the emitting plasma involved. Note that the dynamical time scales at which the reconnection jets evolve might be short compared to the ionization and recombination

times of the ions responsible for the emission in resonance transition region lines. As it will be shown in the next section, the consideration of non-equilibrium ionization is a necessary issue in any related study of explosive events.

Table 4. Series of second order polynomial fits to the radiative loss function of Cook et al. (1989) for photospheric abundances

$\log T$	$\log Q(T) =$
6.5–7.0	$-22.94 + 0.03143 \log T$
6.1–6.5	$-45.634 + 10.02 \log T - 1.000 \log^2 T$
5.9–6.1	$-195.59 + 59.00 \log T - 5.000 \log^2 T$
5.6–5.9	$-53.87 + 11.38 \log T - 1.000 \log^2 T$
5.4–5.6	$-145.54 + 47.35 \log T - 4.500 \log^2 T$
5.1–5.4	$-77.765 + 21.30 \log T - 2.000 \log^2 T$
4.9–5.1	$-145.59 + 49.90 \log T - 5.000 \log^2 T$
4.6–4.9	$-56.897 + 13.425 \log T - 1.250 \log^2 T$
4.3–4.6	$44.60 - 30.49 \log T + 3.500 \log^2 T$
4.0–4.3	$-152.20 + 59.355 \log T - 6.750 \log^2 T$

4.2. Line synthesis

Ionization balance is a valid approximation when a temperature change takes place on time scales greater than the ionization and recombination time scales of the plasma, so that the plasma has had sufficient time to readjust the relative ion populations to the new temperature (see Sarro et al. 1999). However, this is no longer the case with these high velocity jets, and therefore time-dependent ion populations need to be calculated. For this we use the 1-dimensional (1D) code developed and presented in a previous related study where small-scale energy depositions were modelled in 1D radiative hydrodynamics (see, e.g., Sarro et al. 1999). In the present simulations, we consider only the direction along which the largest jet velocities are reached during the 2D MHD experiment, i.e., we reduce the MHD simulations to that viewed along a line-of-sight by a spectrograph. The ion populations were calculated via

$$\frac{\partial N_\mathrm{i}}{\partial t} + v\,\frac{\partial N_\mathrm{i}}{\partial s} = N_\mathrm{e}(N_{\mathrm{i}+1}\alpha_{\mathrm{i}+1} + N_{\mathrm{i}-1}S_{\mathrm{i}-1} - N_\mathrm{i}(\alpha_\mathrm{i} + S_\mathrm{i})) \quad (35)$$

where α_i and S_i are the recombination and ionization coefficients respectively of ionization stage i, and N_i is the number density of ion i. These equations were solved using the values of N_e and T_e provided by the MHD simulations using an adaptive grid algorithm. The ionization and recombination coefficients adopted from Arnaud & Rothenflug (1985) were slightly modified in order to obtain smooth functions of time. Further details and various plots of the derived departure from the equilibrium values are given in Sarro et al. (1999).

Once the ion populations of a given element are computed using this code, the emissivity of a given emission line per unit interval of wavelength in an optically thin, collisionally excited resonance line can be obtained from

$$E_\lambda \propto \frac{hc}{\lambda}\frac{\Omega}{\omega}\frac{N_1}{N_\mathrm{ion}}\frac{N_\mathrm{ion}}{N_\mathrm{elem}}\frac{N_\mathrm{elem}}{N_\mathrm{H}}N_\mathrm{H}N_\mathrm{e}\frac{\exp\frac{-W}{k_\mathrm{B}T}}{\sqrt{T}}\phi(\lambda), \quad (36)$$

where h is the Planck constant, c is the speed of light, Ω is the collisional strength, ω is the statistical weight of the lower level, N_1/N_ion is the ratio of ions responsible for the emission in the ground state relative to the total number of ions per unit volume, $N_\mathrm{ion}/N_\mathrm{elem}$ is the relative population of the ion, $N_\mathrm{elem}/N_\mathrm{H}$ is the element abundance, N_H is the proton density, N_e is the electron density, W is the energy difference between the upper and lower levels, k_B is the Boltzmann constant, T is the temperature, and

$$\phi(\lambda) = \frac{\exp - \left[\frac{(\lambda-\lambda_0-\lambda_\mathrm{s})}{\Delta\lambda_0}\right]^2}{\Delta\lambda_0\sqrt{\pi}}. \quad (37)$$

In the definition of $\phi(\lambda)$, λ_0 is the rest wavelength of the resonance line, and $\lambda_\mathrm{s} = (\frac{\lambda_0}{c})v_\mathrm{p}$ is the Doppler shift corresponding to the velocity of the plasma projected on the line of sight, v_p. The Doppler width of the line $\Delta\lambda_0$ is given by

$$\Delta\lambda_0 = \frac{\lambda_0}{c}\sqrt{\frac{2k_\mathrm{B}T}{m_\mathrm{i}}}, \quad (38)$$

where m_i is the mass of the ion emitting in the resonance line of interest.

By giving the distribution of emissivities along the line of sight, the total intensity can be computed as

$$I(\lambda, t) = \int_0^{S_\mathrm{e}} E(\lambda, s, t)\,\mathrm{d}s, \quad (39)$$

where S_e is the total length of the emitting source projected on the line of sight.

In the numerical experiment described in the previous section, at $t = 0$ s, the absolute value of plasma temperature at the X-point is close to the C IV 1548.2 Å formation temperature. However, this temperature is 3.15 times lower than the temperature of formation of the O VI 1031.9 Å line. Therefore, the "blue-jet" discussed in the previous section will be mainly visible in the O VI resonance line, just because this line has a higher temperature of formation than the C IV line.

To make the "blue-jet" also visible in the time series of the C IV line, we have performed another experiment where the temperature was chosen to be 1.0 10^5 K, rather than 2.0 10^5 K. Also, in order to keep all the model parameters presented in Table 2 unchanged, the typical value of the mass density was increased by a factor of two, as well as the Alfvén velocity being decreased by a factor of $\sqrt{2}$ (and also the Alfvén travel time became $\sqrt{2}$ times longer). Note that after such changes the plasma beta parameter is unchanged. Furthermore, the strength of the magnetic field is the same since the value of the kinetic gas pressure is also unchanged. The differences then only appear

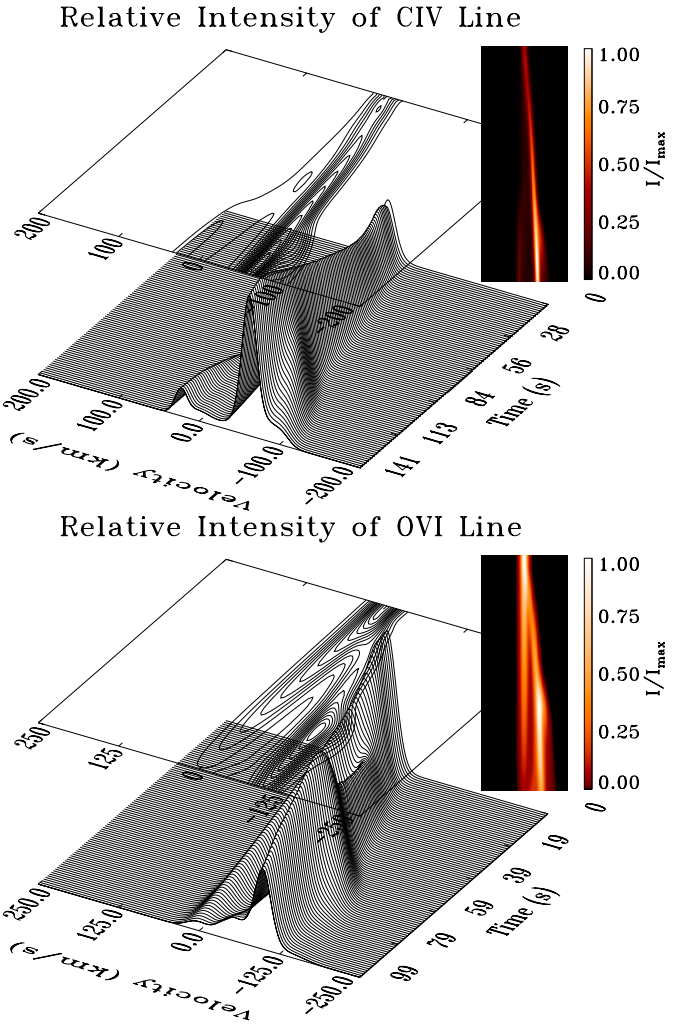

Fig. 5. Time series of the resonance C IV λ1548.2 Å (top), and O VI λ1031.9 Å (bottom) transition region lines are shown. Contour plots represent iso-curves of equal relative line intensity, $I/I_{\max}$. The latter is also shown in grey-scale palette as the image plot at the top right corner of each figure (see text for more details). Notice also that the time is going from right to left

in the radiative loss function, the speed of the thermal conduction, and also the background heating rate.

Figure 5 shows time series of computed line profiles for the 1548 Å resonance line of C IV (top), and 1032 Å line of O VI (bottom), respectively. The time series of the C IV line end at time 141 s, and were obtained when the typical value of the temperature in the MHD experiment was taken as $T_0 = 1.0\ 10^5$ K (which also made the temperature of the X-point become 0.5 times the temperature of formation of the C IV line). The time series of the O VI resonance line end at time 99 s, and were computed using the 2D MHD result of the experiment presented above ($T_0 = 2.0\ 10^5$ K).

In order to perform the line synthesis in 1D, we have chosen the line of symmetry $x = 0$ from the 2D MHD experiment as the line of sight (along which the maximum jet velocities are reached), and averaged the 2D MHD solution over 5 grid points in the $x-$direction. This way we have got a 1D MHD solution which was used as an input to calculate the corresponding ion populations of carbon and oxygen, as well as to compute the line profiles of the two lines discussed above.

The surface plots in Fig. 5 are constructed from individual line profiles computed every 1.0 s. The time along the $x-$axis is given seconds. Also, instead of plotting the line intensity as a function of the wavelength λ, the line profiles are plotted with respect to the corresponding Doppler velocity, $v_{\rm p} = c\,\lambda_{\rm s}/\lambda_0$. The latter is a more representative way to show time series of a given, line revealing velocity events, for example explosive events. Positive velocities represent blue-shifts, whereas negative velocities should be interpreted as red-shifts. The contour plots on top of each surface plot represent the iso-curves of equal relative line intensity $I/I_{\max}(\lambda)$ (where $I_{\max}(\lambda)$ is the maximum line intensity reached during the whole time series). Image plots in grey-scale palette are shown at the top right corner of each figure.

In general, the radiative output from the 1D line synthesis code shown in Fig. 5 can be described as a chain of rapid and short-lived enhancement of the line intensity, followed by the appearance of Doppler shifted components. The blue-shifted component in the O VI line becomes visible when the initial temperature of the X-point is set below the temperature of formation of this line. This applies in a similar manner to the C IV line. For example, when the temperature of the X-point is 1.0 10^5 K, the blue-shifted component (the "blue-jet") will be visible only in the O VI line, whereas the red-shifted component will be dominant in the C IV line. However, at this temperature it is almost impossible to see the "blue-jet" in the C IV line. In turn, when the initial temperature of X-point is set to 5.0 10^4 K, the "blue-jet" becomes also visible in the C IV line.

As one can see in Fig. 5, the blue-shifted component in each line gradually develops in time, reaches a maximum value of the blue-shift, and then remains roughly constant until the end of each time series. The maximum blue-shifts are of the order of 100 km s^{-1} for the C IV line, and 125 km s^{-1} for the O VI line, respectively. On the contrary, the maximum red-shift is of the order of 35 km s^{-1} for the C IV line, and 25 km s^{-1} for the O VI line, respectively.

Our results are in agreement with Sarro et al. (1999) with regard to the necessity of considering "non-equilibrium ionization" in calculating the ion populations. The line synthesis in C IV and O VI presented here, however, reveals different behavior in the computed time series, since the physical situations examined in the two studies are different. Differences also occur in the dynamical time scales involved in the two models. Note that Sarro et al. (1999) examined the 1D HD physical environment (although it implicitly assumed the presence of a magnetic field supporting the loop), while the one involved in the present study is 2D and fully magnetohydrodynamical.

A more detailed analysis of the O VI and C IV lines at various initial temperatures of the X-point will be carried

out in a follow-up paper. We will also perform a parametric scan using various model parameters, as well as examining the corresponding response in the line profiles of these two lines. We believe that the results obtained and presented in this study, although involving a simple 2D model, are on the right track in the modelling of high velocity events, such as explosive events, on the Sun. Also, a detailed line synthesis in various resonance transition region lines would be of key importance in such a study, since it could provide a direct comparison between the results of the numerical modelling with related observations of those transient events.

5. Future work

We are currently in the process of upgrading the "non-equilibrium ionization" code, in order to apply the same scheme described in the previous section to compute the (E)UV line profiles of a few other transition region lines (such as, e.g., C III 977 Å, O V 630 Å, Ne VII 465 Å, and Ne VIII 770 Å emission lines). A direct comparison of such line synthesis with related observations of explosive events will be presented in follow-up papers.

Further improvements of the model and the numerical experiments presented here are in progress. Key issues include:

- Conversion of MHD simulations into directly observable quantities (e.g., emission line profiles) in 2D non-equilibrium ionization;
- Application of a *common* physical model to some other "similar" small-scale transient events of the solar zoo (e.g., blinkers, X-ray jets, seeking a relationship between explosive events and Hα jets);

Ideally speaking, an initial magnetic carpet with Doppler measurements at a photospheric level derived from observations should be taken at $t = 0$, and a numerical experiment would result in phenomena such as explosive events, blinkers, nano/micro-flares, etc. At the present stage of computer resources available we do not think this can be really achieved. Instead, one has to identify the key ingredients of modelling. We also believe one of the most important issues is to convert results of numerical simulations into observable quantities (see Sarro et al. 1999; Erdélyi et al. 1998, 1999; Teriaca et al. 1999 in the 1D HD case).

Acknowledgements. Research at Armagh Observatory is grant-aided by the N. Ireland Dept. of Culture, Arts and Leisure, while partial support for software and hardware is provided by the STARLINK Project which is funded by the UK PPARC. This work was partly supported by a grant from the British Council – Acciones Integradas Program (Spain) ref. No. 1814. I. Roussev dedicates his studies to Ana and Elena. R. Erdélyi is grateful to M. Kéray for patient encouragement. R. Erdélyi acknowledges the financial support obtained from the NSF, Hungary (OTKA, Ref. No. TO32462). K. Galsgaard and I. Roussev are grateful for the warm hospitality they have received during their visits at Space & Atmosphere Research Center (SPARC), Department of Applied Mathematics, University of Sheffield, where part of this work was prepared. I. Roussev is also grateful to the Department of Applied Mathematics, University of St. Andrews, and the NSO in Tucson, Arizona, for the support provided during his visits there. The MHD experiments were carried out on the PPARC-funded Compaq MHD Cluster in St. Andrews.

References

Acton, L., et al. 1992, Science, 258, 618
Arnaud, M., & Rothenflug, R. 1985, A&AS, 60, 425
Browning, P. K. 1991, Plasma Phys. Cont. Nuc. Fusion, 33, 539
Brueckner, G. E., & Bartoe, J.-D. F. 1983, ApJ, 272, 329
Cook, J. W., Cheng, C.-C., Jacobs, V. L., & Antiochos, S. K. 1989, ApJ, 338, 1176
Dere, K. P., Bartoe, J.-D. F., & Brueckner, G. E. 1989, Solar Phys., 123, 41
Dere, K. P., Bartoe, J.-D. F., & Brueckner, G. E. 1991, JGR, 96, 9399
Dere, K. P. 1994, Adv. Space Res., 14(4), 13
Erdélyi, R., De Pontieu, B., & Sarro, L. M. 1999, ESA-SP, 448, 1345
Erdélyi, R., De Pontieu, B., & Roussev, L. M. 2001, ASP Conf. Ser., 223, 619
Erdélyi, R., Doyle, J. G., & Perez, E. P. 1997, ESA-SP, 404, 353
Erdélyi, R., Sarro, L. M., & Doyle, J. G. 1998, ESA SP, 421, 207
Heyvaerts, J., & Priest, E. R. 1983, A&A, 117, 220
Hollweg, J. V. 1984, ApJ, 277, 392
Innes, D. E., Inhester, B., Axford, W. I., & Wilhelm, K. 1997, Nature, 386, 811
Innes, D. E., & Tóth, G. 1999, Solar Phys., 185, 127
Jin, S.-P., Inhester, B., & Innes, D. 1996, Solar Phys., 168, 279
Karpen, J. T., Antiochos, S. K., & Devore, C. R. 1995, ApJ, 450, 422
Narain, U., & Ulmschneider, P. 1996, Space Sci. Rev., 75, 453
Nordlund, Å., & Galsgaard, K. 1995, private communication, `www-solar.mcs.st-and.ac.uk/~klaus/`, A 3D MHD Code for Parallel Computers
Parker, E. N. 1988, ApJ, 330, 380
Perez, M. E., Doyle, J. G., & Erdélyi, R. 1998, ASP Conf. Ser., 154, 666
Perez, M. E., Doyle, J. G., Erdélyi, R., & Sarro, L. 1999, A&A, 342, 279
Porter, J. G., Moore, R. L., Reichman, E. J., Engvold, O., & Harvey, K. L. 1987, ApJ, 323, 380
Priest, E. R., & Forbes, T. G. 1986, JGR, 91, 5579
Rae, C. I., & Roberts, I. 1981, Geophys. Astrophys. Fluid Dyn., 18, 197
Rosner, R., Tucker, W., & Vaiana, G. S. 1978, ApJ, 220, 643
Sarro, L. M. 1998, Ph.D. Thesis
Sarro, L. M., Erdélyi, R., Doyle, J. G., & Perez, E. P. 1999, A&A, 351, 721
Sterling, A. C., Mariska, J. T., Shibata, K., & Suematu, Y. 1991, ApJ, 381, 131
Sturrock, P. A., Dixon, W. W., & Klimchuk, J. A. 1990, ApJ, 356, L31
Teriaca, L., Doyle, J. G., Erdélyi, R., & Sarro, L. M. 1999, A&A, 352, L99
Teriaca, L., Madjarska, M. S., & Doyle, J. G. 2000, A&A, submitted
van Ballegooijen, A. A. 1986, ApJ, 311, 1001
Zirker, J. 1993, Solar Phys., 148, 43